Water incorporation and retention in metamorphic olivine during subduction: Implications for the deep water cycle

Elias D. Kempf*, Jörg Hermann

Institute of Geological Sciences, University of Bern, Baltzerstrasse 3, 3012 Bern, Switzerland

Email: elias.kempf@geo.unibe.ch

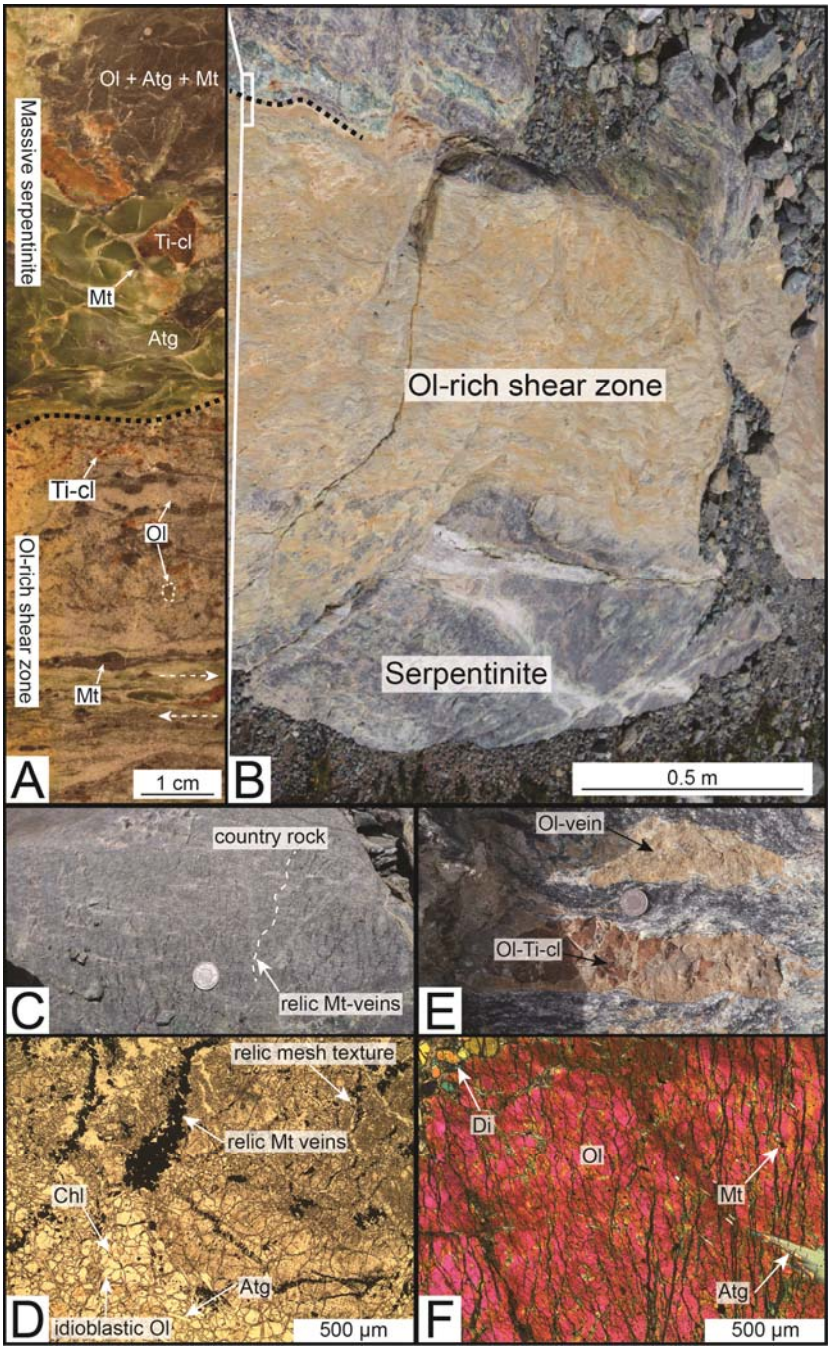

Figure DR1: (A) A polished rock slice showing the nearly undeformed serpentinite and the olivine-rich shear zone below. The sense of shear is indicated with white arrows. (B) Shear zone cutting through a serpentinite. (C) Glacier-polished outcrop of massive country rock serpentinite (FA) with static growth of olivine in a serpentine matrix. Coin (2.3 cm) for scale. (D) Relic magnetite mesh textures are overgrown by large, inclusion-rich olivines that contain variable amounts of sub-micron Ti-clinohumite (Ti-cl) lamellae (thin section microphotograph). The large olivine grains are recrystallized to smaller, clear, idioblastic grains. (E) Outcrop photo of an olivine vein containing

variable amounts of Ti-clinohumite and diopside (Di) (Ol26). (F) Large olivine grains (thin section microphotograph) contain numerous inclusions of antigorite (Atg) and magnetite (Mt) and micron sized chlorites (Chl) only identifyable in EPMA spot analysis mode.

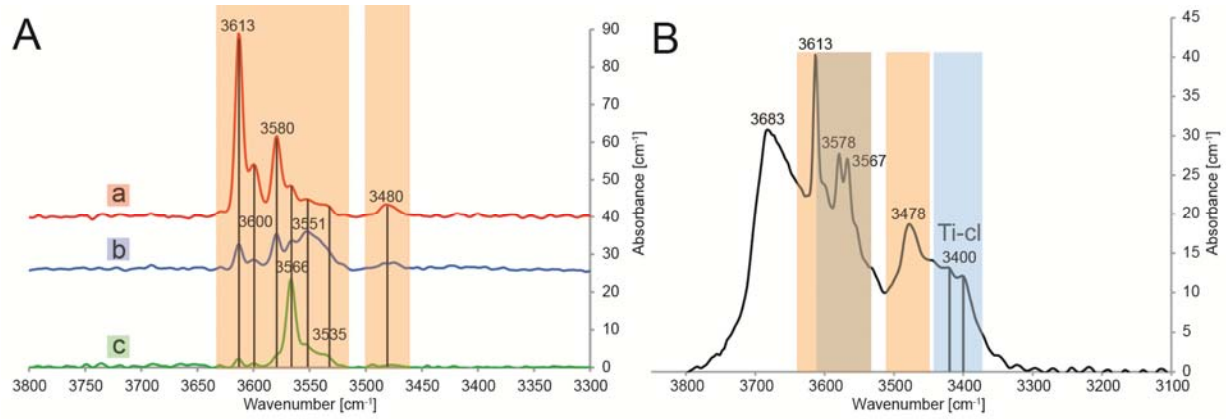

Figure DR2: (A) Characteristic absorption bands of Si-vacancies (orange shaded fields) for each crystallographic orientation a, b and c of olivine grains from the shear zone (Ol1) scaled to 1 cm thickness. The orientations were determined using the Si-O overtones of olivine in polarized FTIR measurements (Asimow et al., 2006). (B) Typical unpolarised FTIR spectrum of a large olivine grain, scaled to 1 cm thickness. The strong absorption is due to contributions from tiny serpentine inclusions (main band at 3683 cm^{-1}). Si-vacancy (orange shaded fields) and Ti-clinohumite lamellae related bands (blue shaded fields) have discrete bands at 3613 cm^{1} and 3400 and 3417 cm^{-1} respectively, and overlap between 3525-3580 cm^{-1}.

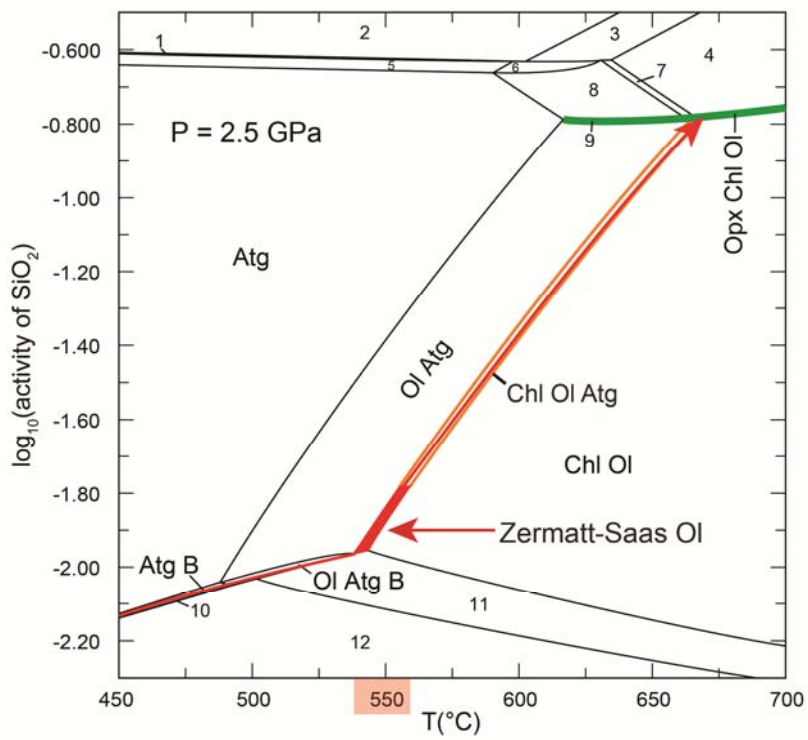

Figure DR3: SiO_2-activity vs temperature diagram calculated at 2.5 GPa with Perplex (Connolly, 2009): The red line shows the increase in SiO_2-activity with increasing temperatures for the assemblages antigorite+brucite; antigorite+brucite+olivine and antigorite+chlorite+olivine. The red area shows the SiO_2-activity equilibrium conditions for the study location, at temperatures just above the brucite-out. The green line shows that the SiO_2-activity is one order of magnitude higher at the orthopyroxene-in reaction. Solution models and corresponding author names in brackets are presented according to Perplex solution_model.dat-file. The numbers represent different assemblages 1: (Chl, T, Atg) 2: (Chl, T) 3: (Opx, Chl, T) 4: (Opx, Chl) 5: (T, Atg) 6: (Opx, T, Atg) 7: (Opx, Chl, Atg) 8: (Opx, Atg) 9: (Opx, O, Atg) 10: (Chl, Atg, B) 11: (Chl, O, B) 12: Chl.

METHODS

Thick sections (approximately 200 µm thickness for Ol1, Ol2, Ol26 and 100 µm for FA) were produced from representative olivine-bearing samples and textures have been investigated by optical microscopy and BSE imaging. Every olivine grain in this study was analysed in the following order: EPMA, FTIR and LA-ICP-MS.

FOURIER TRANSFORM INFRARED (FTIR) SPECTROSCOPY

For FTIR measurements, free-standing double polished 200/100 µm thick sections were measured with a Bruker Hyperion IR microscope in a sample chamber that is continuously flushed by dry air. Most transparent olivine grains were measured with a MCT (Mercury-Cadmium-Telluride) detector connected to a Bruker Tensor IR spectrometer. Measurements were acquired with 64 scans and an effective spectral resolution of 4 cm^{-1}. Acquisition of water distribution maps was obtained with a FPA (Focal Plane Array) detector consisting of 64x64 (4096) points acquired simultaneously. 128 scans and an effective spectral resolution of 8 cm^{-1} were used. Acquired spectra were base-line corrected using the concave rubber band method with 64 points and 4 iterations implemented in the Opus software. The atmospheric water compensation using the Opus software was applied to all spectra. All grains were analysed with polarized and unpolarized light for comparison. The principle axes were determined comparing overtones of the Si-O bonds (2200-1200 cm^{-1}) with end member spectra from Asimov et al. (2006). Water concentration quantification was performed using the B integration method, accomplished with the Bruker OPUS software. Both MCT and FPA spectra were renormalized to 1 cm thickness. The thicknesses of the wavers were measured with a probe (dial) indicator with an accuracy of 1 µm for MCT measurements. For the FPA maps potential variation in thickness was monitored using the integrated overtone approach from Shen et al. (2014). Water contents were calculated with the absorption coefficient from Bell et al. (2003). Characteristic bands were identified according to Padrón-Navarta et al. (2014). Errors given in Table1 follow the protocol given by Demouchy et al. (2015) for a homogeneous population. Taking the observed zonation shown by the FPA-map into account, the variable measurement position in different grains due to small inclusions of hydrous silicates induces a further error of similar extent. Considering only the ±15% error of Demouchy et al. (2015) water concentrations of all samples are within error of each other.

Electron probe micro analyser (EPMA)

Analyses were conducted with a JEOL JXA-8200 Superprobe equipped with a tungsten filament, five wavelength dispersive crystal spectrometers (WDS) and one energy dispersive (EDS) spectrometer. A standard setup of 15 kV acceleration voltage and 20 nA probe current was used. Measurement time was set to 20 s on the peak and 10 s for either peak positions. Natural and synthetic oxide and silicate minerals were used as standards.

Laser ablation inductively coupled mass spectrometry (LA-ICP-MS)

Trace element analyses were accomplished by LA-ICP-MS using a Geolas Pro 193 nm ArF excimer laser system coupled to an ELAN DRC-e quadrupole ICP-MS instrument. Optimization of the instrument and measurement strategies were adapted from Pettke et al. (2012). NIST 610 and 612 glasses were used for optimization of the detectors and the GSD-1G glass was chosen as external standard. The fluence of the laser pulses were set at 6 J/cm^2 with a 10 Hz repetition. The spot sizes were between 60-120 µm in diameter. The background was measured for 50 s. As an internal standard MgO was used from quantitative EPMA analyses (Table DR1). Data reduction was accomplished with the Matlab programme SILLS (Guillong et al., 2008).

THERMODYNAMIC MODELING

The $aSiO_2$ vs. temperature diagram was calculated for a representative bulk rock using Perplex (Connolly, 2009) and is graphically displayed in Figure DR3. The Holland and Powell (1998) data base revised in 2002 was used. The solution models O(HP), Chl(HP), Opx(HP), Band Tare from Holland and Powell (1998), Atg(PN) from Padrón-Navarta et al. (2013), for olivine, chlorite, orthopyroxene, brucite, talc and antigorite, respectively. For the determination of average brucite and olivine contents in serpentinites an average bulk rock composition was calculated from Li et al. (2004) in Table 1 without the “spinel peridotite” samples 20, 21. The volume percent of brucite and olivine were then calculated with the Perplex routine called “meemum” of the Perplex software in the

MgO-FeO-Al_2O_3-SiO_2-H_2O system assuming excess H_2O (MgO: 38.28, FeO: 7.17, Al_2O_3: 2.72, SiO_2: 39.43). The bulk for the shear zone corresponds to the bulk used for phase diagram computation (Fig. DR3), (MgO: 48.86, FeO: 3.25, Al_2O_3: 1.66, SiO_2: 39.65) and is derived from quantitative element mapping.

REFERENCES

Asimow, P. D., Stein, L. C., Mosenfelder, J. L., and Rossman, G. R., 2006, Quantitative polarized infrared analysis of trace OH in populations of randomly oriented mineral grains: American mineralogist, v. 91, no. 2-3, p. 278-284.

Bell, D. R., Rossman, G. R., Maldener, J., Endisch, D., and Rauch, F., 2003, Hydroxide in olivine: A quantitative determination of the absolute amount and calibration of the IR spectrum: Journal of Geophysical Research: Solid Earth, v. 108, no. B2, p. 2015-2113, doi:10.1029/2001JB000679.

Connolly, J., 2009, The geodynamic equation of state: what and how: Geochemistry, Geophysics, Geosystems, v. 10, no. 10.

Demouchy, S., Ishikawa, A., Tommasi, A., Alard, O., and Keshav, S., 2015, Characterization of hydration in the mantle lithosphere: Peridotite xenoliths from the Ontong Java Plateau as an example: Lithos, v. 212, p. 189-201.

Guillong, M., Meier, D. L., Allan, M. M., Heinrich, C. A., and Yardley, B. W., 2008, Appendix A6: SILLS: A MATLAB-based program for the reduction of laser ablation ICP-MS data of homogeneous materials and inclusions: Mineralogical Association of Canada Short Course, v. 40, p. 328-333.

Holland, T., and Powell, R., 1998, An internally consistent thermodynamic data set for phases of petrological interest: Journal of Metamorphic Geology, v. 16, no. 3, p. 309-343.

Li, X. P., Rahn, M., and Bucher, K., 2004, Serpentinites of the Zermatt-Saas ophiolite complex and their texture evolution: Journal of Metamorphic Geology, v. 22, no. 3, p. 159-177.

Padrón-Navarta, J. A., Hermann, J., and O'Neill, H. S. C., 2014, Site-specific hydrogen diffusion rates in forsterite: Earth and Planetary Science Letters, v. 392, p. 100-112.

Padrón-Navarta, J. A., Sánchez-Vizcaíno, V. L., Hermann, J., Connolly, J. A., Garrido, C. J., Gómez-Pugnaire, M. T., and Marchesi, C., 2013, Tschermak's substitution in antigorite and consequences for phase relations and water liberation in high-grade serpentinites: Lithos, v. 178, p. 186-196.

Pettke, T., Oberli, F., Audétat, A., Guillong, M., Simon, A. C., Hanley, J. J., and Klemm, L. M., 2012, Recent developments in element concentration and isotope ratio analysis of individual fluid inclusions by laser ablation single and multiple collector ICP-MS: Ore Geology Reviews, v. 44, p. 10-38.

Shen, T., Hermann, J., Zhang, L., Padrón-Navarta, J. A., and Chen, J., 2014, FTIR spectroscopy of Ti-chondrodite, Ti-clinohumite, and olivine in deeply subducted serpentinites and implications for the deep water cycle: Contributions to mineralogy and petrology, v. 167, no. 4, p. 1-15.